Fluctuation Mitigation and Azimuthal Velocity Profile Regulation by Extremum Seeking in HELCAT

Zeki Okan Ilhan[1], Jason Barry[1], Hexiang Wang[1], Eugenio Schuster[1], Mark Gilmore[2], Andrew Ware[3]

[1]Lehigh University, Bethlehem, PA, USA

[2]University of New Mexico, Albuquerque, NM, USA

[3]University of Montana, Missoula, MT, USA

e-mail: zoi210@lehigh.edu

Abstract— **Turbulence, and turbulence-driven transport are ubiquitous in magnetically confined plasmas, where there is an intimate relationship between turbulence, transport, destabilizing mechanisms like gradients and currents, and stabilizing mechanisms like shear. Active control of fluctuations via manipulation of flow profiles is investigated in a magnetized laboratory plasma device (HELCAT). Measurements of the azimuthal velocity are assumed available at several radial points within the plasma and $E \times B$ flow profiles are controlled via biased ring electrodes. An optimal control algorithm is proposed in this work to reproduce as closely as possible a prescribed desired radial azimuthal velocity profile. The effectiveness of the controller is analyzed via numerical simulations.**

I. INTRODUCTION

Various magnetic confinement devices have been generated so far to carry out wide range of plasma experiments in laboratory environment. Plasma processes usually span wide range of parameters covering several orders of magnitude in density, temperature and magnetic field strength. However, laboratory experiments are in general limited by the range of parameter space the plasma generation mechanism can access. Considering these limitations, the HELCAT (Helicon-Cathode) device (Fig. 1) has been designed and built to access a wide range of parameters in a modest-scale laboratory device [1]. One of the objectives of HELCAT is to establish the feasibility of using advanced control algorithms to control cross-field turbulence-driven particle transport through appropriate manipulation of radial plasma flow profiles [2].

Though many of the detailed physics of the interrelationship between turbulence, transport drive mechanisms and flow remain unclear, there is clear experimental evidence in both fusion and laboratory plasmas that transport and/or turbulence can be suppressed or reduced via shaping of plasma flow profiles (flow shear) [3], [4]. Several theories were proposed to explain this phenomenon. Currently, the most accepted cause for transport mitigation is the reduction and/or stabilization of turbulence by sheared $E \times B$ flow profiles [4]. In the HELCAT device, the $E \times B$ flow (or, azimuthal flow, V_θ) is generated by the azimuthal force created by the interaction of the axial magnetic field (B) due to the magnets surrounding the plasma column and the radial

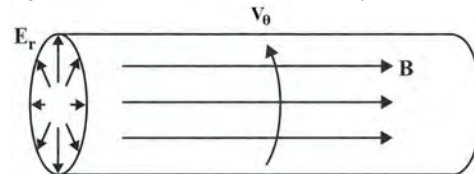Fig. 1. The HELCAT device at University of New Mexico.

Fig. 2. Azimuthal flow in a magnetized plasma column [5].

electric field (E_r) imposed by the set of biased concentric ring electrodes that terminate the plasma column (Fig. 2).

In previous work by the authors, a multi-parameter, extremum-seeking, adaptive controller has been designed to mitigate the plasma fluctuations in HELCAT [2]. This previous result is extended in this work by designing an optimal controller that achieves an azimuthal flow profile as close as possible to a prescribed target profile. Measurements of the azimuthal flow velocity are assumed available at several radial points within the plasma. The resulting optimal control problem is addressed by using the extremum seeking algorithm [6] with a cost functional that represents the error between actual and target azimuthal flow profiles.

This paper is organized as follows. The HELCAT plasma device is briefly described in Section II. The transport model implemented in the predictive code for HELCAT is introduced in Section III. The proposed extremum seeking algorithm is introduced and results of some numerical simulations are provided in Section IV. Finally, the paper is ended by a brief conclusion and a statement of future goals in section V.

Fig. 3. Left: Helicon source during operation in helium. Center: Cathode source. Right: Copper concentric bias rings mounted on ceramic substrate.
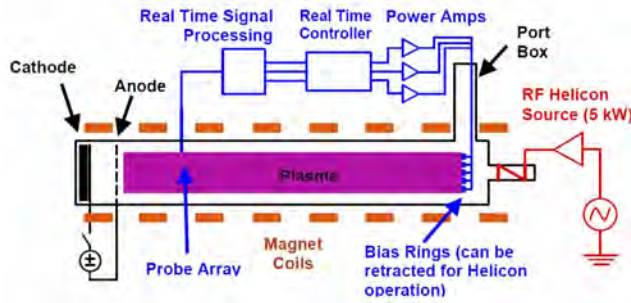

Fig. 4. Schematic of HELCAT feedback control system.

II. A DESCRIPTION OF THE HELCAT PLASMA DEVICE

The HELCAT (Helicon-Cathode) linear plasma device at University of New Mexico (UNM), shown in Fig. 1, consists of a 4 m long, 50 cm diameter cylindrical stainless steel vacuum chamber in two 2 m sections. Each section has eight 10 in, twelve 8 in, and fourteen 3.375 in conflat type ports providing excellent diagnostic access. Currently four 10 in gate valves and seven KF-40 differentially pumped linear probe feedthroughs provide diagnostic access while under vacuum. Magnetic fields are produced by a total of thirteen water-cooled solenoidal magnetic coils (steady state magnetic fields of up to 2.2kG at 500 A) [1].

HELCAT is a dual-source plasma device that makes use of two different sources with different ionization mechanisms. These are the helicon RF source and the thermionic cathode sources located at the two ends of the vacuum chamber (Fig. 3). The helicon source is usually characterized by producing high density plasmas with peaked profiles and relatively long discharge times. On the other hand, the cathode source is capable of producing lower density plasmas with broader profiles and shorter discharge times. Cathode sources also generate hotter plasmas when compared to helicon sources. Although each source can be operated separately, with both sources acting simultaneously, it is possible to operate HELCAT over a wide range of plasma collisionalities (via changes in background neutral pressure).

A typical hardware configuration used for real-time measurement and control in the HELCAT device is depicted in Fig. 4 above. There are 6 concentric bias rings located at the helicon end of the plasma column. The voltages of the bias rings are control inputs for the control system to manipulate the $E \times B$ flow profiles. The configuration of the bias rings

are shown in Fig. 3. The rings are located on a ceramic substrate and are separated by gaps of approximately 7 mm. Ring radii are 3.0, 3.7, 4.4, 5.1, 5.9 and 6.6 cm. A set of four 400 W Kepco BOP-20-20M power operational amplifiers, which can source or sink up to 20 A at 20 V with a 10 kHz/20 V slew rate, are available for fast ring biasing. Also, several 12 V car batteries can be used to apply DC bias to rings.

The real time controller hardware contains set of rack mounted DTACQ ACQ196CPCI compact PCI digitizers (32 channels, 500 Ksamples/sec, 12 bits), with an on board embedded Linux system. This system is controlled by a host PC running Linux and Labview. For real time control, the system is operated in "low latency" mode, which allows 32 inputs to be read, control decisions made, and outputs written in 120 μs. [2].

III. TRANSPORT MODEL

Transport models are used to describe the qualitative response of the plasma profiles to the actuators (concentric bias rings) for a specified scenario. Recent models have included neoclassical and turbulent transport processes as well as the interplay between pressure gradients, flow generation, and radial electric field shear. In this section, the transport model developed by Newman, Lopez-Bruna et al [7] is introduced. This model predicts the radial-temporal evolution of the flux-surface averaged density, $n(r,t)$, electron temperature, $T_e(r,t)$, ion temperature, $T_i(r,t)$, axial velocity, $V_z(r,t,)$, azimuthal velocity, $V_\theta(r,t)$, RMS fluctuation amplitude, $\varepsilon(r,t)$, and radial electric field, $E_r(r,t)$, where r and t respectively denote the radial and temporal variables.

The evolution of the density is governed by

$$\frac{\partial n}{\partial t} = s + \frac{1}{r}\frac{\partial}{\partial r}\left[rD_n \frac{\partial n}{\partial r} \right], \qquad (1)$$

where s is the power deposition profile, which is modeled by a flat-top radial profile, i.e.,

$$s(r) = \begin{cases} S_0, & r \le w_s, \\ 0, & r > w_s, \end{cases} \qquad (2)$$

where w_s is the radial width of the source and S_0 is the cathode/helicon source. The term D_n on the right hand side of (1) is the total particle diffusivity, which includes both neoclassical and turbulent effects. It is modeled by

$$D_n = D_0 + \mu_{\text{prof}} D_{0_b} \sqrt{\frac{T_e}{\left| \frac{1}{T_e}\frac{\partial T_e}{\partial r} + \frac{1}{n}\frac{\partial n}{\partial r} \right|}} \, \epsilon^2, \qquad (3)$$

where D_0 (collisional particle transport coefficient), D_{0_b} (turbulent particle transport coefficient) and μ_{prof} (turbulent transport profile modification) are all constants.

The evolution of the electron temperature, $T_e(r,t)$, and the ion temperature, $T_i(r,t)$, are governed by the following two partial differential equations (PDEs):

$$\frac{3n}{2}\frac{\partial T_e}{\partial t} = s\frac{E_{0e}}{T_{e0}} + \frac{1}{r}\frac{\partial}{\partial r}\left[r\left(D_{T_e}n\frac{\partial T_e}{\partial r} + \frac{5}{2}D_nT_e\frac{\partial n}{\partial r}\right)\right]$$
$$+D_n\frac{1}{n}\frac{\partial n}{\partial r}\frac{\partial nT_i}{\partial r} - q_b\sqrt{\frac{1}{T_e}}n^2\left(1 - \frac{T_{i0}T_i}{T_{e0}T_e}\right) \quad (4)$$

$$\frac{3n}{2}\frac{\partial T_i}{\partial t} = s\frac{E_{0i}}{T_{i0}} + \frac{1}{r}\frac{\partial}{\partial r}\left[r\left(D_{T_i}n\frac{\partial T_i}{\partial r} + \frac{5}{2}D_nT_i\frac{\partial n}{\partial r}\right)\right]$$
$$-D_n\frac{1}{n}\frac{\partial n}{\partial r}\frac{\partial nT_i}{\partial r} + q_b\sqrt{\frac{1}{T_e}}n^2\left(\frac{T_{e0}}{T_{i0}} - \frac{T_i}{T_e}\right) - \mu_{cx}nT_i, \quad (5)$$

where the electron and ion power sources (E_{0e} and E_{0i}, respectively), the electron and ion normalization factors (T_{e0} and T_{i0}), the ion-electron energy exchange factor, q_b and the normalized charge exchange flow damping factor, μ_{cx} are all constants. The first terms on the right hand sides of (4)-(5) represent the cathode electron and ion energy inputs, respectively. The second terms reflect the summation of conductive and convective energy fluxes. The third terms are describing the ion-electron friction while the fourth terms represent the ion-electron energy transport. Finally, the additional last term on the RHS of (5) represents the charge-exchange damping.

The axial velocity equation is

$$\frac{\partial V_z}{\partial t} = \alpha_z\frac{\partial}{\partial r}\left(r^2\epsilon\frac{\partial\epsilon}{\partial r}\frac{\partial E_r}{\partial r}\right) + sV_{z0in} - \mu V_z$$
$$+\frac{1}{r}\frac{\partial}{\partial r}\left(rD_{V_z}\frac{\partial V_z}{\partial r}\right), \quad (6)$$

where α_z (the axial flow generation parameter), V_{z0in} (the axial momentum input from the source) and μ (the flow damping multiplier) are all constants and D_{V_z} is the diffusivity of the axial velocity. By definition, $D_{V_z} = D_n$, where D_n is given by (3). The first term on the right hand side of (6) is related to the Reynolds stress flow generation, the second term represents the axial momentum source from the helicon, third term represents the charge-exchange flow damping and the last term is related to the flux divergence of the axial velocity.

The poloidal, or azimuthal, flow equation is

$$\frac{\partial V_\theta}{\partial t} = S_\theta - \mu V_\theta + \frac{1}{r}\frac{\partial}{\partial r}\left[rD_{V_\theta}\frac{\partial V_\theta}{\partial r}\right]$$
$$+\alpha_\theta\frac{\partial}{\partial r}\left[r^2\epsilon\frac{\partial\epsilon}{\partial r}\frac{\partial E_r}{\partial r}\right]\left(\frac{2}{r^2 f_{ac}}\right), \quad (7)$$

where S_θ is the azimuthal flow (momentum) source, D_{V_θ} is the diffusivity of the azimuthal velocity, α_θ is the azimuthal flow generation parameter and f_{ac} is the Reynolds stress suppression term. Note that the azimuthal flow diffusivity, D_{V_θ}, is modeled in the same way as the total particle diffusivity, D_n in (3), with D_0 ten times greater, D_{0b} fifty

times greater, and the same μ_{prof}. The Reynolds stress suppression term, f_{ac}, is a function of the plasma radius given by

$$f_{ac}(r) = 1 + 10^{-6}\left[\frac{1}{(1.000001 - r)^6} + \frac{1}{(0.000001 + r)^6}\right] \quad (8)$$

The evolution equation for the radial electric field is governed by

$$E_r = \alpha_{diag}.\alpha\left(\frac{\partial T_i}{\partial r} + T_i\frac{1}{n}\frac{\partial n}{\partial r}\right) - V_{\theta_{norm}}V_\theta, \quad (9)$$

where α_{diag} is the factor used to turn-off the diamagnetic effects on E_r, α is the normalization factor for the diamagnetic terms and $V_{\theta_{norm}}$ is the normalization factor for the azimuthal flow.

Finally, the evolution of the RMS fluctuation is governed by

$$\frac{\partial\epsilon}{\partial t} = \left\{\gamma - \alpha_{\epsilon_1}\alpha_1\epsilon\left|\frac{1}{n}\frac{\partial n}{\partial r}\right|^{-\frac{1}{4}} - \alpha_{\epsilon_2}\left[r\frac{\partial}{\partial r}\left(\frac{E_r}{r}\right)\right]^2\right\}\epsilon$$
$$+\frac{1}{r}\frac{\partial}{\partial r}\left[rD_\epsilon\frac{\partial\epsilon}{\partial r}\right], \quad (10)$$

where $\varepsilon \equiv \sqrt{<(\tilde{n}/n)^2>}$ ($\tilde{n}$ is the density fluctuation), D_ϵ is the diffusivity of the turbulence, which equals the total particle diffusivity given in equation (3), γ is the growth rate factor given by

$$\gamma = g\gamma_0\nu_{ei}T_e\left(\frac{1}{n}\frac{\partial n}{\partial r}\right)^2, \quad (11)$$

where g is the time normalization factor, γ_0 is the growth rate multiplier and ν_{ei} is the electron-ion collision rate. The growth rate factor in (11) is defined based on the theory of drift wave instabilities in helicon plasmas [8]. The turbulent saturation factor, α_{ϵ_1}, normalization factor, α_1, and the shear suppression factor, α_{ϵ_2}, are all constants. The first term on the right hand side of (10) represents the fluctuation drive (growth rate), the second term is related to the nonlinear energy transfer (saturation), the third term is the $E \times B$ shear suppression, and the last term represents the diffusion of fluctuations.

The actual control inputs for the HELCAT experiments are the voltages of the biased concentric rings. Their effect can be reproduced by using localized, Gaussian, momentum sources in the predictive transport code. The azimuthal flow source term is then governed by the following model:

$$S_\theta(r) = \sum_{j=1}^{6}p_c(j)\exp\left\{\frac{-[r_p(j) - r]^2}{2[w_{pc}(j)]^2}\right\}, \quad (12)$$

where p_c (momentum source strengths), r_p (radial positions of the momentum source), and w_{pc} (momentum source widths) are all six dimensional arrays that describe the characteristics of the gaussian momentum source.

The actual bias ring positions of the HELCAT device are 0.2, 0.24666667, 0.29333333, 0.34, 0.39333333 and 0.44 in normalized radius w.r.t. the plasma radius. For $p_c(j) = 1$ and $w_{pc}(j) = 0.028 \; \forall j = 1, ..., 6$, the azimuthal momentum
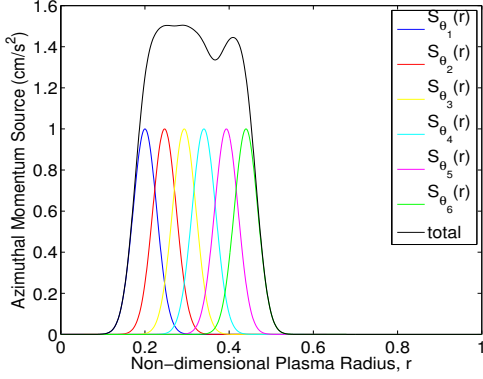
Fig. 5. Gaussian momentum sources.

source is shown in Fig. 5. The black curve represents the total azimuthal flow source, $S_\theta(r)$, while the individual contributions of the bias rings are shown by the separate curves plotted in color.

IV. EXTREMUM SEEKING OPTIMAL CONTROL

A. Fundamentals of the Extremum Seeking Algorithm

Extremum seeking can be applied in nonlinear problems if the nonlinearity has a local minimum or maximum. The origin of the nonlinearity may be due to the plant itself or due to the control objective imposed on the plant in the form of a cost functional of an associated optimization problem. Therefore, extremum seeking is applicable either for finding the set point that corresponds to the optimal output, or for tuning the parameters of a feedback control law [6]. The former application is used in this paper to achieve a target azimuthal velocity profile for the HELCAT device by regulating the momentum sources provided by the concentric bias rings.

In numerical studies, the to-be-optimized vector parameter θ consists of the azimuthal momentum source strengths, $p_c(j)$, in (12). The value of the vector θ is changed systematically after each plasma "discharge." In a simulation environment, the term discharge refers to the integration of the PDEs described in Section III. Since the variable θ is changed or tuned after each plasma simulation, it is convenient to apply the discrete time version of the extremum seeking algorithm [6], [9]. The implementation of the extremum seeking control scheme is depicted in Fig. 6, where z stands for the Z-transform variable. The static nonlinear block $J(\theta)$ in Fig. 6 represents in this work the accumulated error between the target and achieved azimuthal velocity profiles after each plasma run. Hence, the control objective is to minimize J. The variable θ^* represents the minimizing values of θ, while J^* represents the corresponding minimum value of the cost function, J. Therefore, $J^* = J(\theta^*)$.

The objective of the extremum seeking algorithm is then to drive $\theta - \theta^*$ to zero in order to drive $J(\theta)$ to its optimal value, J^* [6]. The variable $\hat{\theta}$ in Fig. 6 represents the estimation of the unknown optimal input θ^*. The probing signal $a\cos(\omega k)$, which is added to the estimate $\hat{\theta}$ and then fed into the plant, yields a measure of the gradient information of the
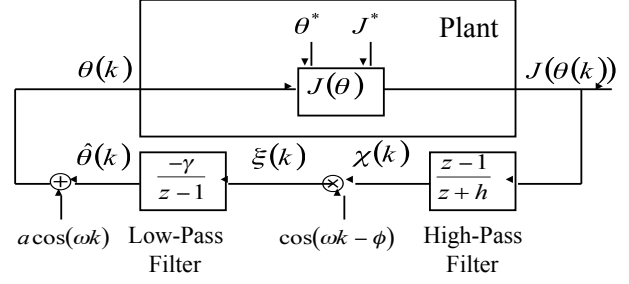

Fig. 6. Extremum seeking control scheme for discrete-time systems.

map $J(\theta)$. The role of the high-pass filter is to extract only the perturbation in the cost functional J caused by the perturbation in the θ parameter created by the probing signal. The effect of the demodulation, $cos(\omega k - \phi)$, is to reveal only the component of the filtered perturbed cost functional χ having the same frequency ω as the probing signal. Finally, the signal ξ is fed into the pure-integrator low-pass filter to update the θ parameter in order to drive the cost functional J to its minimum [9]. The discrete time extremum seeking algorithm shown in Fig. 6 can be summarized as follows

$$\chi(k) = -h\chi(k-1) + J(k) - J(k-1) \quad (13)$$
$$\xi(k) = \chi(k)\cos(\omega k - \phi) \quad (14)$$
$$\hat{\theta}(k+1) = \hat{\theta}(k) - \gamma\xi(k) \quad (15)$$
$$\theta(k+1) = \hat{\theta}(k+1) + a\cos(\omega(k+1)). \quad (16)$$

The high-pass filter, $\frac{z-1}{z+h}$, is designed as $0 < h < 1$, and the modulation frequency ω is selected such that $\omega = \alpha\pi$, $0 < |\alpha| < 1$, where α is rational. It is important to select ω large in a qualitative sense when compared with the plant time scale. The cut-off frequencies of the filters need to be lower than the frequency ω of the probe signal. These observations impose constraints and, at the same time, a relationship between ω and h. As an additional constraint, ω should not equal any frequency present in the measurement noise. The perturbation amplitude a needs to be small in order to make the steady state output error also small. Given a, the adaptation gain γ of the low pass filter needs to be small enough to preserve stability [6], [9].

In this case we are dealing with a multi-parameter extremum seeking procedure. Note that, as described in Section II, only 4 power supplies are available in the actual HELCAT machine. Hence, only four out of the six bias rings can be controlled independently. Therefore, the extremum seeking variables are defined to have 4 components given by

$$\theta(k) = \begin{bmatrix} \theta_1(k) \\ \theta_2(k) \\ \theta_3(k) \\ \theta_4(k) \end{bmatrix}, \; \hat{\theta}(k) = \begin{bmatrix} \hat{\theta}_1(k) \\ \hat{\theta}_2(k) \\ \hat{\theta}_3(k) \\ \hat{\theta}_4(k) \end{bmatrix}, \; \xi(k) = \begin{bmatrix} \xi_1(k) \\ \xi_2(k) \\ \xi_3(k) \\ \xi_4(k) \end{bmatrix}$$

Similarly, the perturbation terms are

$$cos(\omega k) = \begin{bmatrix} cos(\omega_1 k) \\ cos(\omega_2 k) \\ cos(\omega_3 k) \\ cos(\omega_4 k) \end{bmatrix}, \; cos(\omega k + \phi) = \begin{bmatrix} cos(\omega_1 k + \phi_1) \\ cos(\omega_2 k + \phi_2) \\ cos(\omega_3 k + \phi_3) \\ cos(\omega_4 k + \phi_4) \end{bmatrix}$$
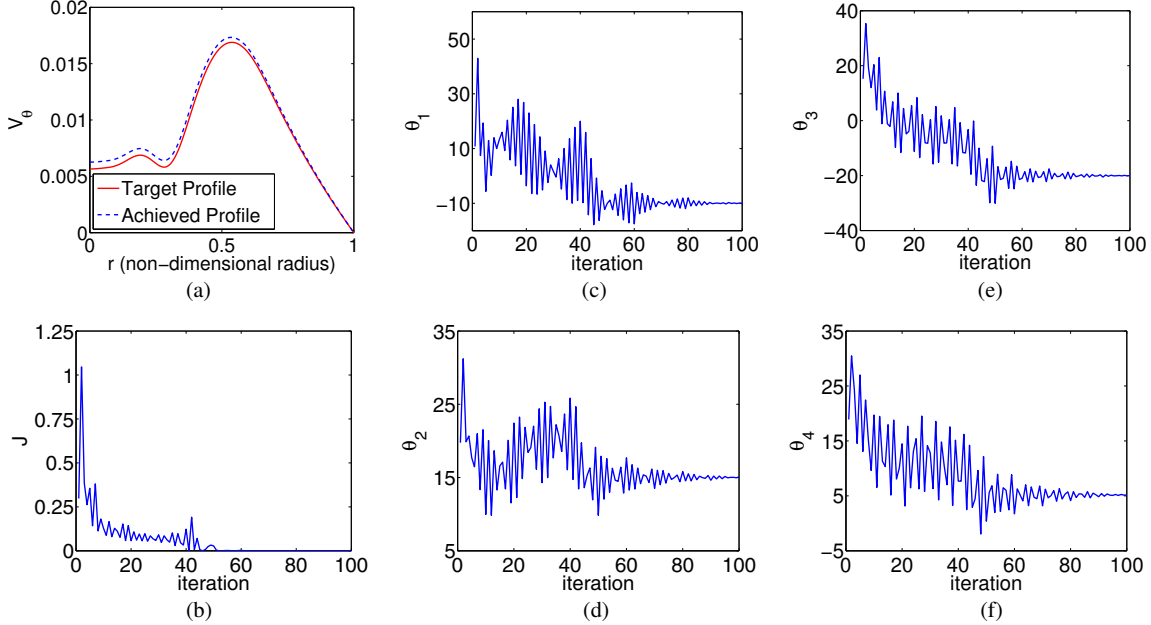
Fig. 7. (a) Target and achieved (by the extremum-seeking controller) V_θ flow profiles at $t = 250$ ms for iteration $k = 100$; (b) Evolution of the cost function, $J(k)$; (c)-(f) Evolutions of the extremum seeking variables $\theta_1 = p_c(1)$, $\theta_2 = p_c(2)$, $\theta_3 = p_c(3)$, $\theta_4 = p_c(4)$.

The extremum seeking constants in Fig. 6 are diagonal matrices given by

$$a = \begin{bmatrix} a_1 & 0 & 0 & 0 \\ 0 & a_2 & 0 & 0 \\ 0 & 0 & a_3 & 0 \\ 0 & 0 & 0 & a_4 \end{bmatrix}, \quad \gamma = \begin{bmatrix} \gamma_1 & 0 & 0 & 0 \\ 0 & \gamma_2 & 0 & 0 \\ 0 & 0 & \gamma_3 & 0 \\ 0 & 0 & 0 & \gamma_4 \end{bmatrix}$$

For this application, we define the cost function as

$$J = \sqrt{\int_0^{r_a} [V_\theta(r,T) - V_\theta^*(r)]^2 \, dr}, \qquad (17)$$

where $V_\theta^*(r)$ is the target azimuthal velocity profile at $T = 250$ ms and $r_a = 15$ cm is the plasma radius. In each iteration k of the extremum seeking procedure, we fix $\theta(k)$ and obtain direct or indirect measurements of the azimuthal velocity profile at N points along the plasma radius, i.e., $V_\theta(r_i, T)$ for $i = 1, \ldots, N$. The definite integral in (17) can then be discretized approximately as

$$J(k) = J(\theta(k)) \approx \sqrt{\sum_{i=1}^{N} [V_\theta(r_i, T) - V_\theta^*(r_i)]^2}, \quad (18)$$

Equation (18) is then fed into the extremum-seeking algorithm, (13)-(16) to compute $\theta(k+1)$.

B. Numerical Simulations

The effectiveness of the proposed extremum seeking controller is tested through numerical simulations using the predictive transport code for HELCAT introduced in Section III. For this purpose, a target azimuthal velocity profile is generated by setting the azimuthal momentum source strengths (p_c) to the following arbitrary values:

$$p_c = [-10 \ \ 15 \ -20 \ \ 5 \ \ 5 \ \ 5]^T \qquad (19)$$

In the actual HELCAT device, only four out of the six bias rings can be controlled independently. Hence, the extremum seeking algorithm is designed to regulate only four source strengths while the two additional source strengths are fixed at the values associated with the target profile given in (19). We define

$$\theta = [\theta_1 \ \ \theta_2 \ \ \theta_3 \ \ \theta_4]^T = [p_{c1} \ \ p_{c2} \ \ p_{c3} \ \ p_{c4}]^T \qquad (20)$$

At each iteration k of the extremum seeking algorithm, $\theta(k)$ is fixed and the associated cost functional $J(\theta(k))$ is calculated using the simulated discharge. The extremum seeking algorithm generates the actuator waveforms to drive the azimuthal velocity profile close to the selected target profile. Fig. 7(a) shows the target V_θ profile together with the profile achieved by the extremum seeking controller at the end of the simulated discharge (250 ms simulation) after 100 iterations. The azimuthal velocity profile V_θ flow is in normalized (i.e., non-dimensional) form. Fig. 7(b) shows the evolution of the cost functional, $J(\theta(k))$, as a function of the extremum seeking iterations. It is seen from Fig. 7(a)-(b) that the extremum seeking controller tracks the target profile after around 100 iterations as the cost functional almost becomes zero. Fig. 7(c)-(f) show the evolutions of the extremum seeking parameters, θ_i, for $i = 1, \ldots, 4$, which are the first four channels of the azimuthal momentum source strengths. It can be noted from these figures that the source strengths estimated by the extremum seeking controller indeed converge to the values associated with the target profile in (19).
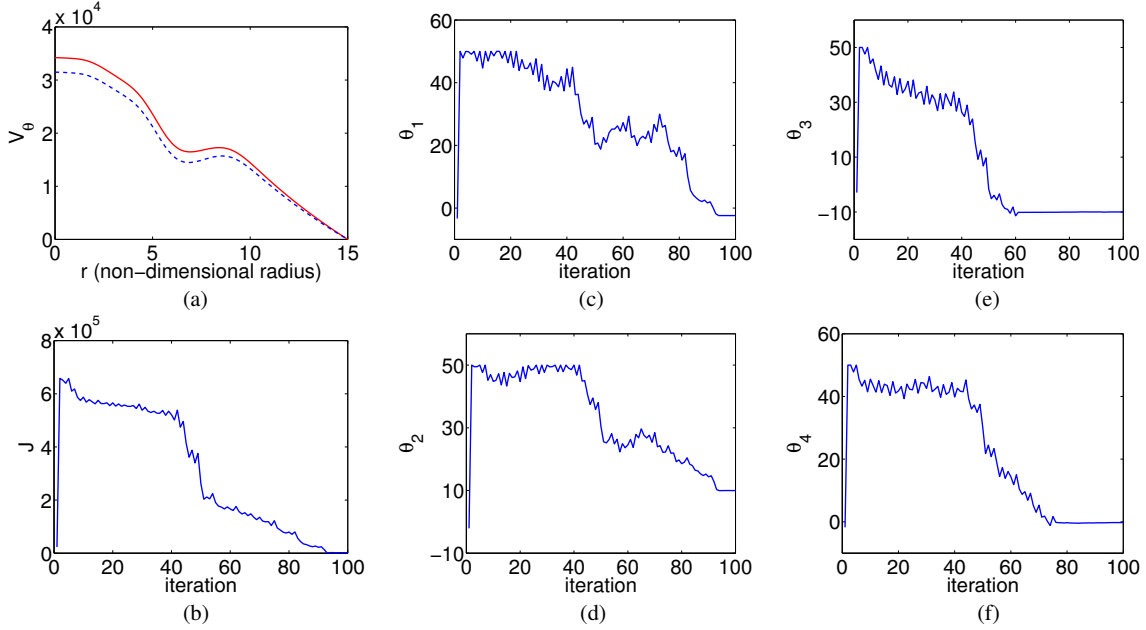
Fig. 8. (a) Target V_θ flow profile and actual profile achieved by the extremum-seeking controller (at $t = 250$ ms, for iteration 100). (b) Evolution of the cost function, $J(k)$. (c)-(f) Evolutions of the extremum seeking variables: $\theta_1 = p_c(2)$, $\theta_2 = p_c(3)$, $\theta_3 = p_c(4)$, $\theta_4 = p_c(5)$.

Another extremum seeking simulation study is performed by generating the target azimuthal velocity profile using the following values for the the azimuthal momentum source strengths (p_c):

$$p_c = [10 \ -2 \ 10 \ -10 \ 0 \ 5]^T \qquad (21)$$

In this case, the first and last input channels are fixed while the inner four channels are regulated by the extremum seeking controller, i.e., we define

$$\theta = [\theta_1 \ \theta_2 \ \theta_3 \ \theta_4]^T = [p_{c2} \ p_{c3} \ p_{c4} \ p_{c5}]^T \qquad (22)$$

As can be seen from Fig. 8(b), the cost function is relatively larger in magnitude when compared to the case with the normalized V_θ flow (Fig. 7(b)). This makes the tuning of the algorithm more challenging. However, it is seen from Fig. 8(a) that the extremum seeking controller is still effective in matching the target profile after around 100 iterations. Fig. 8(c)-(f) show the actuator waveforms, which show that the source strengths estimated by the extremum seeking controller converge to the values used for the generation of the target profile and given in (21).

V. CONCLUSIONS

A four-parameter, extremum-seeking, adaptive controller has been designed to find the control inputs (azimuthal momentum strength sources) that are necessary to achieve a target azimuthal flow profile in the HELCAT linear plasma device. The controller parameters have been tuned using a predictive transport code under development for HELCAT. Based on the results of the numerical simulations, the control algorithm is shown to be effective in shaping the azimuthal flow profile in HELCAT. The goal is to implement the extremum-seeking controller in the actual HELCAT device as soon as the capability of measuring in real time the azimuthal flow at different radial locations becomes available (a multi-point probe is currently under development). The non-model-based nature of the extremum controller is a clear advantage when transitioning from simulation to experiment. When implemented in HELCAT, the extremum-seeking controller will regulate not the momentum strengths but the ring voltages. Moreover, the controller will take into account constraints on the control inputs (voltage rings), which were neglected in this work.

REFERENCES

[1] A. G. Lynn, M. Gilmore, C. Watts, J. Herrea, R. Kelly, S. Will, S. Xie, L. Yan, and Y. Zhang, "The HelCat dual-source plasma device," *Review of Scientific Instruments*, vol. 80, no. 103501, 2009.

[2] Q. Wang, E. Schuster, M. Gilmore, S. Xie, and A. Ware, "Extremum-Seeking-Based Fluctuation Mitigation by ExB Actuation in HELCAT," in *Proceedings of the 5th IEEE Multi-conference on Systems and Control, Denver, Colorado*, September 28-30 2011.

[3] P. W. Terry, "Suppression of Turbulence and Transport by Sheared Flow," *Reviews of Modern Physics*, vol. 72, no. 1, pp. 109–165, 2000.

[4] N. Crocker, G. Y. Burin, M. J. Burin, G. R. Tynan, B. P. Cluggish, and K. R. Umstadter, "Control of Velocity Shear and Turbulence Through Biasing in CSDX," *Program of the 44th Annual Meeting of the APS Division of Plasma Physics*, vol. 47, p. 264, 2002.

[5] D. Gurnett and A. Bhattacharjee, *Introduction to Plasma Physics*. Cambridge University Press, 2003.

[6] K. Ariyur and M. Krstic, *Real-Time Optimization by Extremum Seeking Feedback*. Wiley, 2005.

[7] D. E. Newman, B. A. Carreras, D. Lopez-Bruna, P. H. Diamond, and V. B. Lebedev, "Dynamics and control of internal transport barriers in reversed shear discharges," *Physics of Plasmas*, vol. 5, no. 4, pp. 938–952, 1998.

[8] R. F. Ellis, E. Marden-Marshall, and R. Majeski, "Collisional drift instability of a weakly ionized argon plasma," *Plasma Physics*, vol. 22, pp. 113–132, 1980.

[9] K. A. J. Choi, M. Kristic and J. Lee, "Extremum seeking control for discrete-time systems," *IEEE Transactions on Automatic Control*, vol. 47, no. 2, pp. 318–323, 2002.